Low-temperature structural instabilities of the halide double perovskite $Cs_2AgBiBr_6$ investigated via x-ray diffraction and infrared phonons

Collin Tower,* Fereidoon S. Razavi, Jeremy Dion, and Maureen Reedyk
Department of Physics, Brock University, St. Catharines, Ontario, Canada

Jürgen Nuss and Reinhard K. Kremer
Max Planck Institute for Solid State Research, Stuttgart, Germany

(Received 19 December 2024; accepted 26 May 2026; published 10 June 2026)

The halide double perovskite $Cs_2AgBiBr_6$ has been proposed as a potential replacement for organic halide perovskites for photovoltaic applications. Further investigation of its dielectric response, optical properties, and structural stability is thus warranted. $Cs_2AgBiBr_6$ exhibits a well-documented structural phase transition at 120 K but indications for an additional lower-temperature (∼40 K) phase transition have also been reported. On the basis of measurements of the specific heat capacity, temperature-dependent powder x-ray diffraction, low-frequency capacitance, and infrared reflectivity, we clarify the previously reported splitting of phonon modes in the Raman spectrum at ∼40 K as due to a subtle structural phase transition from the tetragonal $I4/m$ structure to a monoclinic $P12_1/n1$ crystal structure. The infrared-active vibrational modes are experimentally investigated in the three structural regimes. In the cubic structure at room temperature, the four infrared-active modes are observed at 135, ∼85, 55, and ∼25 cm^{-1}. As the symmetry reduces to tetragonal, a minute splitting of these modes is found; however, below 40 K additional mode splitting is observed, indicating a further reduction in symmetry.

DOI: 10.1103/fs84-8lgj

I. INTRODUCTION

Halide perovskite materials have come into increased scientific focus due to their potential for photovoltaic device applications such as in solar cell technology [1] or x-ray detection devices [2]. Lead halide perovskites with the composition $A^+Pb^{2+}X_3^-$, where A^+ can be an organic cation, typically methylammonium (MA), formamidinium, or an alkali cation, and X^- is a halide anion with Cl^-, Br^-, and I^-, are broadly investigated examples. While $MAPbI_3$ has reached noteworthy photovoltaic efficiencies, its integration into photovoltaic devices has been held back by issues of thermal instability [3] and ecological concern over the incorporation of toxic lead [4]. As the thermal stability of inorganic materials is typically higher than that of organic materials, the former problem is addressed by replacing the organic cation with an inorganic alkali metal such as Cs. Inorganic halide perovskites, however, still exhibit stability issues through structural transformations and oxidization [5].

*Contact author: ct15zs@brocku.ca

Published by the American Physical Society under the terms of the Creative Commons Attribution 4.0 International license. Further distribution of this work must maintain attribution to the author(s) and the published article's title, journal citation, and DOI.

Substitution with less toxic elements with the same valence electron configuration as lead such as tin and germanium has been investigated. However, due to the higher energy of their outer *s* orbitals, these materials readily oxidize to a nonphotoactive state [6]. Bi^{3+} offers a less toxic alternative to lead with the same orbital structure. However, to substitute Pb^{+2} with trivalent Bi^{3+}, the composition must be modified by adding a monovalent cation to maintain charge neutrality. The resulting double perovskites have the composition $A_2BB'X_6$, where A and B are monovalent metal cations, typically Cs and Cu, Ag, or Au, respectively, B′ is a trivalent pnictogen, such as Sb or Bi, and X is a halide Cl^-, Br^-, or I^- anion [7]. The Goldschmidt tolerance and octahedral factors suggest that Ag^+ has an ideal ionic radius for creating stable octahedral coordination with Br and I [8], and as such, a halide double perovskite that has garnered great interest is $Cs_2AgBiBr_6$. There is a well-documented structural phase transition in $Cs_2AgBiBr_6$ where upon lowering temperature the crystal structure changes from a highly symmetric cubic structure space group $Fm\bar{3}m$ to a tetragonal crystal structure. This transition occurs at around ∼120 K and affects many of the optoelectronic properties, including the exciton energy, the band gap, and the carrier lifetime [9]. From neutron powder diffraction data, Schade *et al.* refined the crystal structure at 30 K assuming the tetragonal space group $I4/m$ [9].

The low-temperature structural behavior of $Cs_2AgBiBr_6$ was further investigated by Keshavarz *et al.* who noted a peak in the thermal expansion coefficient at ∼40 K and proposed that it was due to an additional structural anomaly of unknown origin [10]. In contrast to the 120 K structural phase transition causing a sharp anomaly in the heat capacity (C_P), Keshavarz *et al.* reported that the ∼40 K transition could not be seen in heat capacity measurements, while Cohen *et al.* detected it in the first temperature derivative of C_P and proposed that it is weakly first order [11]. He *et al.* carried out extensive x-ray and neutron diffraction measurements to investigate this low-temperature phase transition and suggested that it is caused by a phonon instability of the tetragonal phase creating a complex ground state with a very large unit cell comprising several hundred atoms [12].

The double perovskites have been predicted to have ultralow thermal conductivity attributed to strong anharmonicity in their vibrational properties. For $Cs_2AgBiBr_6$, this strong anharmonicity has been suggested to be the cause of the cubic-to-tetragonal phase transition due to the occurrence of a soft phonon branch [13,14]. The Raman-active phonons of $Cs_2AgBiBr_6$ as it passes through both phase transitions have been thoroughly studied experimentally [11]. Splitting of some and a number of additional Raman modes were observed, suggesting a symmetry lowering of the crystal structure below 40 K, possibly to a monoclinic crystal structure. The infrared (IR) phonon spectrum has been predicted via theoretical density functional theory (DFT) calculations [15].

Herein, we study experimentally the effect of the structural instabilities in $Cs_2AgBiBr_6$ on its IR optical properties via the far-infrared vibrations. Knowledge of the IR-active modes imparts further insight into the optical properties of $Cs_2AgBiBr_6$ and provides valuable information that can aid first-principles calculations of the phonon dispersion as experimental values can be compared with the calculated values to evaluate the accuracy of the DFT calculations and refine the parameters used. As the crystals are centrosymmetric, the IR-active modes determined experimentally in this work together with the complementary Raman-active modes that have been measured extensively, for example, by Cohen *et al.* [11], give the nearly complete phonon frequencies at the gamma point. As phonons carry thermal energy, they play an important role in properties such as the heat capacity, thermal conductivity, expansion, and transport. Confidence in DFT predictions of such properties will thus be aided by full knowledge of the experimentally determined gamma point frequencies.

We have measured the IR-active modes and analyzed the results using the Kramers-Kronig (KK) analysis. The results agree reasonably well with the theoretical DFT predictions [13–16]. Additional phonon modes below the ∼40 K structural transition are observed in the IR spectra. To gain further insight, we performed extensive low-temperature x-ray powder and single-crystal diffraction measurements. These confirm the structural phase transition from a cubic to a tetragonal crystal structure at ∼120 K. Subtle signatures are seen in various quantities (cell volume, lattice parameters) consistent with an additional structural phase transition below ∼40 K. Taking into account the additional Raman modes found below ∼40 K by Cohen *et al.* [11] and the appearance

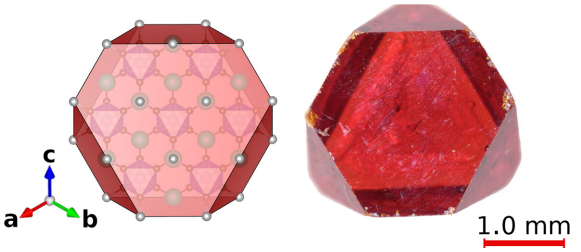


FIG. 1. Left: An example crystal geometry of $Cs_2AgBiBr_6$ taken along the eight permutations of the (111) plane. Right: A crystal synthesized using the controlled cooling method.

of the additional IR modes we observe below 40 K, we are led to conclude that the low-temperature crystal structure is monoclinic and can be described in space group $P12_1/n1$.

II. EXPERIMENTAL

Crystals of $Cs_2AgBiBr_6$ were synthesized following the controlled cooling method outlined by Yin *et al.* [17]. Details are included in the Supplemental Material [18]. A typical crystal is shown in Fig. 1. In order to check for impurities, a random selection of crystals was crushed and checked by powder x-ray diffraction (PXRD) at room temperature. Figure 2 shows a room-temperature powder x-ray diffraction pattern of $Cs_2AgBiBr_6$ in comparison with a Rietveld profile refinement assuming space group $Fm\bar{3}m$. The pattern collected using Co Kα_1 radiation ($\lambda = 1.789\,010$ Å) proves absence of impurities or splitting of Bragg reflections at high Bragg angles assuring cubic symmetry at room temperature.

Heat capacity and capacitance measurements at 50 Hz were carried out with a physical property measurement system (Quantum Design) from 4 to 300 K. The dielectric permittivity was determined from the capacitance. Further details can be found in the Supplemental Material [18].

The lattice parameters of $Cs_2AgBiBr_6$ were determined as a function of temperature from profile refinements (Rietveld refinement [19]) of powder x-ray diffraction patterns collected of two powder samples with a Bruker D8 Discovery x-ray diffractometer system (Bragg-Brentano scattering geometry) using monochromatized Cu Kα_1 radiation). One powder sample was prepared by mildly crushing small crystals in an agate mortar. The particle size of the sample was adjusted between 32 and 63 μm by straining the powder through sieves of the respective mesh size. The

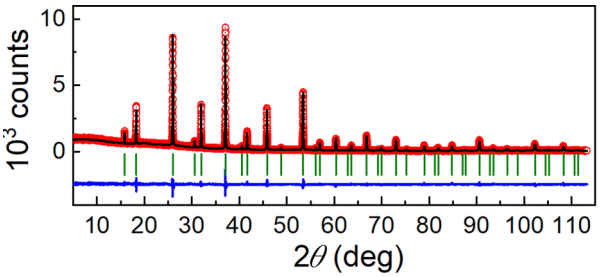


FIG. 2. PXRD pattern of a powder specimen obtained by crushing crystals of $Cs_2AgBiBr_6$, collected at 298 K using Co Kα_1 radiation ($\lambda = 1.789\,010$ Å). The red circles display the measured data, and the black solid line represents the pattern calculated using the positions of the Bragg angles indicated by the green vertical bars. The blue solid line highlights the difference between measured and calculated patterns. Cs, Ag, Bi, and Br atoms occupy Wyckoff sites 8c, 4b, 4a, and 24e, respectively, in space group no. 225 ($Fm\bar{3}m$) with $Z = 4$ (see Table III).

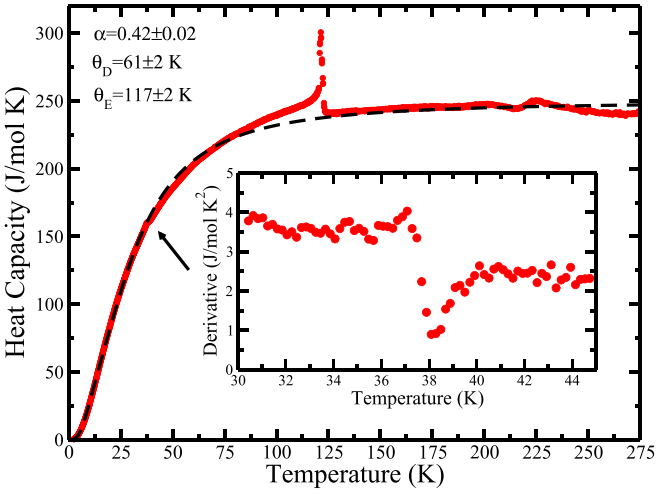


FIG. 3. The heat capacity of $Cs_2AgBiBr_6$ displaying a sharp anomaly at ∼120 K. The inset shows the numerical derivative with respect to temperature, which manifests as a slight inflection in the heat capacity near ∼38 K.

second sample was prepared from a powder formed in lieu of bulk crystals in one of our synthesis attempts. Additional information can be found in the Supplemental Material [18].

Low-temperature single-crystal x-ray diffraction measurements were performed at select temperatures using Mo Kα_1 radiation with cooling via an Oxford Cryosystems device [20]. The reflection intensities were integrated with the SAINT subroutine available in the Bruker Suite software [21]. An absorption correction [22] was applied and the crystal structures were solved by direct methods and full-matrix least-squares fitting using standard software (SHELXTL, JANA2006) [23–25]. For more details, see Ref. [18].

Temperature-dependent IR reflectance was measured over a range of 20–11 000 cm^{-1} using a Bruker-IFS-66v/s Fourier transform spectrometer with in-house modifications for temperature control. Details of the source, detector, and beam splitter combinations used can be found in the Supplemental Material [18]. The sample was annealed at 100 °C for several days before the IR measurements were performed to ensure that it was free of water contamination, as prior to annealing the midinfrared (MIR) range showed evidence thereof. See the Supplemental Material for further details [18]. The absolute reflectivity was determined by using a metallic film deposited on the sample surface *in situ* as in Ref. [26]. Kramers-Kronig analysis was performed to transform from the experimentally determined reflectivity spectra to the complex dielectric function.

III. RESULTS AND DISCUSSION

A. Heat capacity

The heat capacity of $Cs_2AgBiBr_6$ as a function of temperature is shown in Fig. 3. It displays a pronounced λ anomaly near 120 K due to the crystal structure transition from cubic to tetragonal ($Fm\bar{3}m \rightarrow I4/m$) described previously by Schade *et al.* [9]. An analog anomaly near ∼40 K is not observed in the direct heat capacity data. However, the derivative with respect to the temperature reveals an inflection near ∼38 K (see inset in Fig. 3) corresponding well to the temperature below which, e.g., additional Raman peaks were detected [11].

The heat capacity was fit to a weighted Einstein and Debye model given by Eq. (1). The model includes three parameters: a weight factor between the Debye and Einstein model α, and the Debye and Einstein temperatures θ_D and θ_E. T is the temperature, R is the ideal gas constant, and N is the

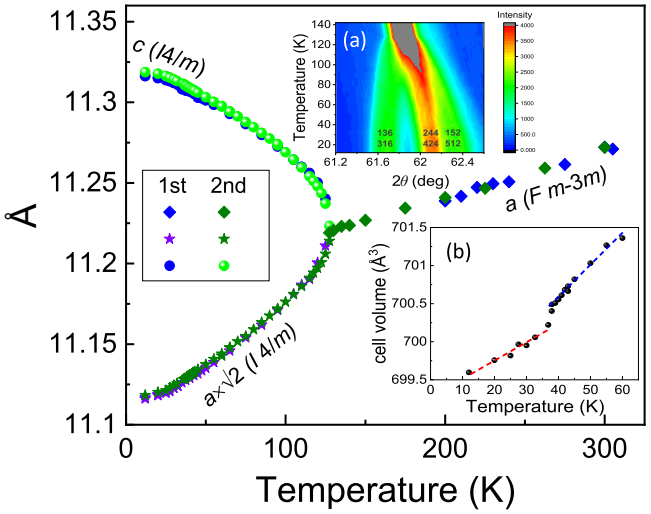


FIG. 4. Lattice parameters as a function of temperature as obtained by Rietveld profile refinements of two sets of x-ray diffraction patterns collected using x-rays of wavelength of $\lambda = 1.540\,598$ Å. Inset (a) displays a contour plot highlighting the splitting of the $(642)_{\text{cubic}}$ Bragg reflection below ∼120 K. The inscribed Bragg indices are with respect to the tetragonal space group $I4/m$. Inset (b) shows the temperature dependence of the tetragonal cell volume below 60 K. The dashed lines are guides to the eye.

number of atoms in the formula unit.

$$C_p = 9\alpha NR\left(\frac{T}{\theta_D}\right)^3 \int_0^{\theta_D/T} \frac{x^4 e^x}{(e^x-1)^2} dx + 3(1-\alpha)NR\left(\frac{\theta_E}{T}\right)^2 \frac{e^{\theta_E/T}}{(e^{\theta_E/T}-1)^2}. \quad (1)$$

This fit, with parameters given in Fig. 3, agrees well at low temperatures deviating slightly at the ∼40 K phase transition, then deviating significantly at the 120 K structural phase transition before recovering at the high-temperature Dulong-Petit law value of ∼250 J/(mol K) just above the 120 K tetragonal-to-cubic phase transition. The features observed in the experimental curve near 220 K are attributed to anomalies in the heat capacity of the Apiezon N Vacuum Grease [27]. The fit converged to a 42% ± 2% Debye contribution signifying that the acoustic phonons have a slightly weaker contribution than the optical phonons to the heat capacity.

The Einstein and Debye temperatures found above agree reasonably well with experimental and theoretical determinations of the phonon frequencies. The Debye frequency of 42 ± 1 cm^{-1} is comparable to the maximum acoustic phonon frequency of ∼50 cm^{-1} determined by the DFT calculations of Zelewski *et al.* [16]. The Einstein frequency of 81 ± 1 cm^{-1} is in good agreement with the average of the experimental optical phonon frequencies of 91 cm^{-1}, as derived from the room-temperature Raman data reported by Cohen *et al.* [11] and the infrared modes identified in this study.

B. Low-temperature crystal structure

A first approach to explore the low-temperature crystal structure of $Cs_2AgBiBr_6$ was made based on PXRD patterns collected between room temperature and 12 K on two samples obtained by crushing a set of larger crystals and a polycrystalline powder formed in lieu of bulk crystals in one synthesis attempt. Initially, the powder diffraction patterns were analyzed by Rietveld profile refinements assuming the tetragonal space group $I4/m$ for $T < 120$ K and $Fm\bar{3}m$ for $T > 120$ K. Within error bars, the lattice parameters of the two samples (see Fig. 4) are identical and correspond well to those reported before by Schade *et al.* [9]. The splitting of the lattice parameters at ∼120 K

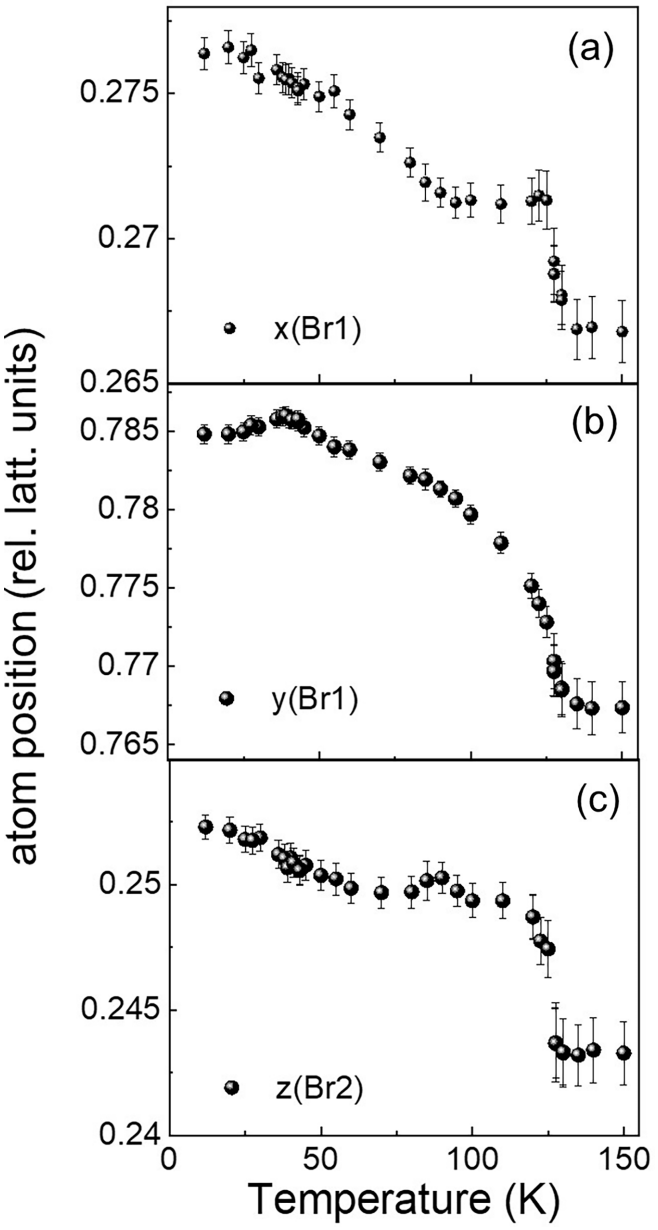


FIG. 5. Atom positional parameters x, y of the Br1 [panels (a) and (b)] and z of the Br2 atoms [panel (c)] in $Cs_2AgBiBr_6$ as obtained from Rietveld profile refinements of the powder diffraction data collected using Cu Kα_1 radiation assuming space group $I4/m$.

reflects the cubic-to-tetragonal structural phase transition. The Br atom positional parameters also respond to the cubic-to-tetragonal structural phase transition. In Figs. 5(a)–5(c), we summarize the x, y, and z positional parameters of the bromine atoms labeled Br1 and Br2, respectively. All exhibit a clear increase below ∼125 K.

Below ∼40 K, the profile refinements assuming the space group $I4/m$, requiring a splitting of the single Br cubic site into two sites (Br1 and Br2), also fit the diffraction patterns fairly well, indicating

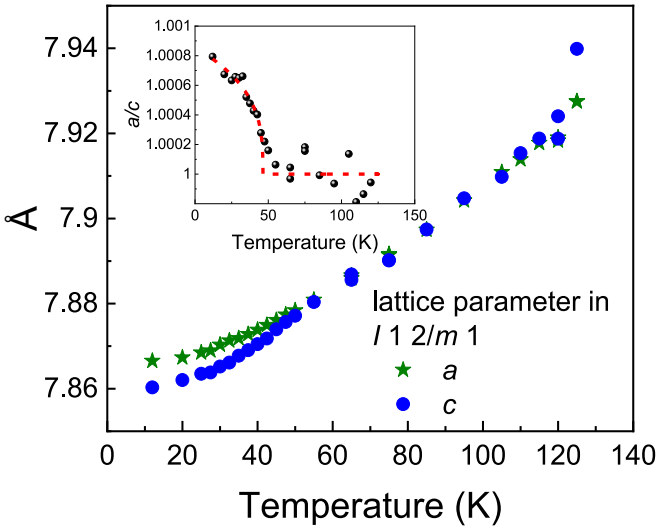


FIG. 6. Lattice parameters a and c obtained from Le Bail fits [28] of the x-ray powder diffraction patterns [assuming the monoclinic space group $I12/m1$ (space group no. 12)]. The inset shows the ratio a/c. The red dashed line is a fit to a critical power law indicating a critical temperature $T_{c,\mathrm{mono}} \approx 46$ K.

no dramatic symmetry lowering of the crystal structure, in agreement with the finding reported by Schade *et al.* [9]. However, while changes in the $I4/m$ refined lattice parameters at around 40 K are not immediately evident, the temperature dependence of the cell volume exhibits a decrease and slight change of slope at this temperature [see Fig. 4(b)]. This finding is paralleled by an anomaly of the atom positional parameter y of the Br1 atoms (Wyckoff site 8h—see Table III) at the same temperature (see Fig. 5). Whereas y of Br1 atom passes through a peak at 38 K, the x positional parameter tends to saturation below this temperature. Similarly, the z positional parameter of the Br2 atoms (Wyckoff site 4e) levels off, reaching a value of 0.2523(5) in the temperature region below 40 K.

The single-crystal x-ray structure analysis (for more details, see the Supplemental Material [18]) confirms the tetragonal space group $I4/m$ for the crystal structures at 60 and 100 K. Also, an intensity dataset collected at 32 K can be readily refined assuming tetragonal symmetry and space group $I4/m$. A similarly acceptable refinement can, however, also be achieved in the triclinic space group $I\bar{1}$. This finding, along with the anomalies observed in the heat capacity, the cell volume, and the bromine atom positional parameters, suggested attempting a refinement of the powder diffraction patterns collected below 40 K assuming lower than tetragonal symmetry.

Motivated by the commonly encountered double perovskite transformation from $I4/m$ to $I12/m1$ (see the Supplemental Material for a discussion of phase transitions in double perovskites [18]), we first performed Le Bail fits of the powder diffraction patterns assuming monoclinic symmetry ($I12/m1$, space group no. 12) to trace minute changes of the lattice parameters as a function of temperature [28]. Figure 6 displays the a and c lattice parameters as a function of temperature obtained from the Le Bail fits of the powder diffraction patterns ($\lambda = 1.540\,598$ Å) assuming the special setting of monoclinic space group $I12/m1$ (no. 12). These correspond to the lattice parameter $a = b$ in the tetragonal system. While the fitted lattice parameters a and c are identical between 120 and ~50 K, a minute splitting develops at lower temperatures. The temperature dependence of the splitting ratio a/c (see inset in Fig. 6) is similar to that of a critical power law with a critical temperature of ≈46 K. For $T \to 0$, the splitting amounts to ≈0.1% and the monoclinic angle β becomes 89.931(2)° (see also Table I, third column from left).

TABLE I. Structural parameters of $Cs_2AgBiBr_6$ as obtained from a Rietveld profile refinement of the PXRD pattern collected at 20 K (wavelength Cu Kα_1). As discussed in the main text, four different space groups commonly found for double perovskites were imposed. Error bars are quoted if isotropic displacement parameters B were refined. In some cases, isotropic displacement parameters of the Br atoms were constrained to be identical. Isotropic displacement parameters marked with an asterisk result from an anisotropic refinement assuming $\beta_{12} = \beta_{13} = \beta_{23} = 0$.

Space group	$I\bar{1}$	$I12/m1$	$P12_1/n1$	$I4/m$
No.	2	12	14	87
a (Å)	7.9374(3)	7.8702(2)	7.8603(3)	7.86 409(7)
b (Å)	7.9265(3)	11.3182(2)	7.8672(3)	7.86 409(7)
c (Å)	11.1266(4)	7.8584(2)	11.3179(2)	11.3181(2)
α (°)	90.017(4)	90	90	90
β (°)	89.914(4)	89.931(2)	90.106(2)	90
γ (°)	91.031(2)	90	90	90
V_{cell} (Å^3)	699.96(5)	700.00(3)	699.88(4)	699.96(1)
Cs				
x	0.500(4)	0.5	0.4882(7)	0.5
y	0.500(3)	0.2526(8)	1.000(5)	0.0
z	0.250(2)	0	0.2546(3)	0.25
B_{iso} (Å^2)	0.82(3)	0.65(4)	1.26(5)	0.85(3)*
Ag				
x	0	0	0	0
y	0.5	0.5	0	0
z	0	0	0.5	0.5
B_{iso} (Å^2)	0.23(12)	0.2	0.2	0.2
Bi				
x	0.5	0	0	0
y	0	0	0	0
z	0	0	0	0
B_{iso} (Å^2)	1.08(9)	0.69(4)	1.78(5)	0.76(4)*
Br1				
x	0.252(4)	0	0.978(1)	0.2834(6)
y	0.248(4)	0.2491(7)	−0.00(1)	0.7785(6)
z	1.000(6)	0	0.2508(7)	0
B_{iso} (Å^2)	0.95(5)*	0.84(5)	1.27(9)	1.10(3)
Br2				
x	0.244(3)	0.281(1)	0.287(4)	0
y	0.744(3)	0	0.218(4)	0
z	0.027(1)	0.216(1)	−0.001(4)	0.2495(7)
B_{iso} (Å^2)	0.95(5)*	0.84(5)	2.65(6)	1.10(3)
Br3				
x	0.536(3)	0.225(1)	0.729(3)	–
y	0.037(3)	0	0.233(4)	–
z	0.246(2)	0.716(1)	1.001(4)	–
B_{iso} (Å^2)	1.6(1)*	1.5(1)	2.65(6)	–
R_P (%)	11.6	11.8	13.3	12.3
R_F (%)	9.2	10.7	15.4	10.8
χ^2	20.5	20.0	24.4	22.6

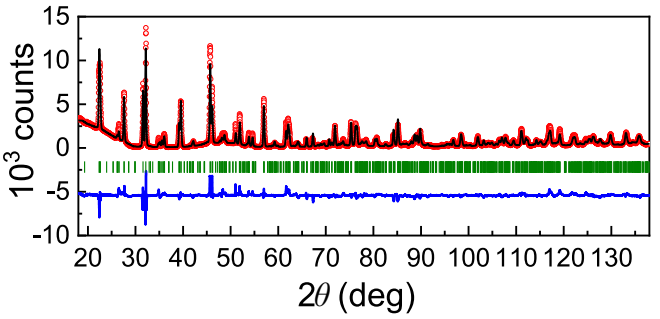


FIG. 7. PXRD pattern of a sample of crushed crystals of $Cs_2AgBiBr_6$ collected at 20 K using Cu Kα_1 radiation ($\lambda = 1.540\,598$ Å). The red circles display the measured data, and the black solid line represents the pattern calculated using the positions of the Bragg angles indicated by the green vertical bars. The blue solid line below highlights the difference between measured and calculated patterns. Cs, Ag, Bi, and Br atoms occupy Wyckoff sites 4e, 2b, 2a, and 4e, respectively, in space group no. 14, setting $P12_1/n1$ (see Table III).

Another frequently observed low-temperature monoclinic crystal structure $P12_1/n1$ resulted in refinements with reliability parameters very close to those of the tetragonal structure with reliability parameters comparable to those of the refinement in the monoclinic space group $I12/m1$. This observation and the examples of the transition metal oxide double perovskites discussed in the Supplemental Material [18] prompted us to try a profile refinement of the powder diffraction patterns collected below ~40 K assuming the space group $I\bar{1}$, which leads to a slight reduction of the reliability factors compared to the refinement using space group $I12/m1$ and a minute cell distortion away from the (almost) orthorhombic cell found with the space group $I12/m1$ or $P12_1/n1$. For the sake of clarity (all angles remain close to 90° in setting $I\bar{1}$), we carried out the refinements in the $I\bar{1}$ setting of the triclinic space group $P\bar{1}$.

Figure 7 displays the powder diffraction pattern collected at 20 K in comparison with the Rietveld profile refinement assuming the space group $P12_1/n1$. Figure 8 displays the corresponding crystal structure of $Cs_2AgBiBr_6$ ($P12_1/n1$ setting of the monoclinic space group no. 14).

The differences between the tetragonal, monoclinic, and triclinic structure solutions refined are minute. Checking the triclinic structure solution with the platon software identified a possible tetragonal super-symmetry $I4/m$ [29]. Tables I and II summarize the structure parameters and the calculated interatomic distances at 20 K in comparison with those obtained from the refinements assuming space group $P12_1/n1$.

To discern a likely crystal structure out of the candidate symmetry groups investigated via Reitveld refinement, optical measurements were taken into consideration. Based upon the Raman-active modes identified by Cohen *et al.* [11] and the results of our infrared spectroscopy investigation presented below, we conclude that $P12_1/n1$ best explains the experimental vibrational spectra.

C. Dielectric permittivity

The temperature dependence of the low-frequency limit complex dielectric function

$$\tilde{\epsilon} = \epsilon_1 + i\epsilon_2, \tag{2}$$

where ϵ_1 and ϵ_2 are its real and imaginary parts, respectively, was extracted from the dielectric capacitance and loss measured between 5 and 300 K at a frequency of 50 Hz using Eqs. (3) and (4):

$$\epsilon_1 = \frac{C}{\epsilon_o}\frac{t}{A}, \tag{3}$$

$$\epsilon_2 = \frac{1}{\epsilon_o \omega}\frac{1}{R}\frac{t}{A}. \tag{4}$$

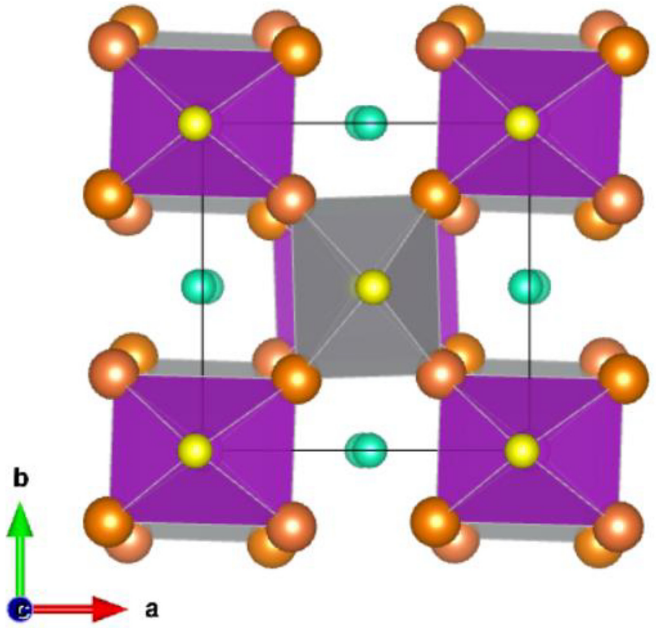


FIG. 8. Crystal structure of $Cs_2AgBiBr_6$ projected along [001] as refined from the PXRD pattern collected at 20 K. The refinement was done assuming monoclinic symmetry (space group no. 14, $P12_1/n1$) assuming isotropic displacement parameters for all atoms. The Br atoms are represented by the yellow (Br1) and the orange (Br2 and Br3) spheres. The Ag and Bi atoms center the Br octahedra depicted in gray and violet, respectively. Cs atoms are shown as cyan spheres.

The system was modeled as a capacitor in parallel with a resistor, where ω is the frequency, and C and R are, respectively, the measured frequency-dependent capacitance and resistance. A is the average area of the sample faces, t is the distance between the faces, and ϵ_o is the permittivity of free space.

Changes in the crystal structure of a material may affect its dielectric response. Neutron scattering measurements have shown that the cubic-tetragonal structural phase transition in $Cs_2AgBiBr_6$ occurs before the soft optic mode frequency becomes zero suggesting the phase transition is weakly first order [30]. The Lyddane-Sachs-Teller equation relates the dielectric properties to the phonon frequencies, predicting that a complete collapse of the soft mode to zero frequency would be accompanied by a divergence in the permittivity [31]. With the soft-mode frequency remaining finite, an anomaly might be expected at the phase transition temperature.

As shown in Fig. 9, the 120 K structural phase transition is present as a clear change in the slope in the real part of the 50 Hz dielectric permittivity and as a peak in its derivative shown overlaid as the orange curve. The slight hysteresis between warming and cooling [see Fig. 9(d)] agrees with the assignment of a weak first-order phase transition. Whereas anomalous behavior near 40 K is not readily visible in the real part of the dielectric response, a change of the slope is clearly observed in the derivative with respect to temperature.

As displayed in Fig. 9(c), the 50 Hz dielectric function was subsequently used to determine the normal incidence reflectivity $\mathbf{R}$ of $Cs_2AgBiBr_6$ via Eq. (5) by taking the magnitude squared of both sides. The reflectivity $\mathbf{R}$ was then used to guide the low-frequency extrapolation of the Kramers-Kronig analysis on $Cs_2AgBiBr_6$, which will be described in detail below:

$$\sqrt{\mathbf{R}}e^{i\theta} = \frac{\sqrt{\tilde{\epsilon}} - 1}{\sqrt{\tilde{\epsilon}} + 1}. \tag{5}$$

TABLE II. Interatomic distances for $Cs_2AgBiBr_6$ as obtained from a Rietveld profile refinement of the PXRD pattern collected at 20 K (see Fig. 7, wavelength Cu Kα_1) assuming monoclinic (space group no. 14, $P12_1/n1$) and triclinic symmetries (space group no. 2, $I\bar{1}$). Distances have been calculated using the atom fractional coordinates and lattice parameters listed in Table I.

Atoms	Distances (Å) ($P12_1/n1$)	Distances (Å) ($I\bar{1}$)
Cs-Br1	3.85(1)	3.927(54)
Cs-Br1	3.94(9)	3.930(54)
Cs-Br1	3.95(9)	3.934(54)
Cs-Br1	4.01(1)	3.937(54)
Cs-Br2	3.79(4)	3.756(33)
Cs-Br2	3.71(4)	3.761(33)
Cs-Br3	3.82(4)	3.677(34)
Cs-Br3	3.90(4)	3.715(340)
Ag-Br1	2.826(8) (2×)	2.852(40) (2×)
Ag-Br2	2.78(3) (2×)	2.731(24) (2×)
Ag-Br3	2.81(3) (2×)	2.846(16) (2×)
Bi-Br1	2.84(1) (2×)	2.807(40) (2×)
Bi-Br2	2.83(3) (2×)	2.863(24) (2×)
Bi-Br3	2.81(3) (2×)	2.773(16) (2×)

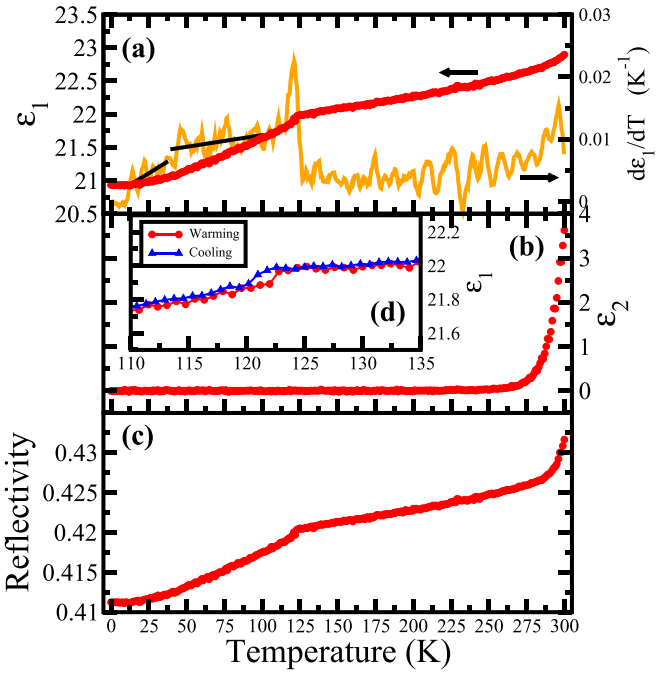


FIG. 9. (a) Temperature dependence of the real part of the dielectric function measured at 50 Hz and its derivative with arrows pointing to their respective axes. The black straight lines are fits to the derivative data above and below the low-T phase transition. (b) Temperature dependence of the imaginary part of the dielectric function measured at 50 Hz. The dielectric function was subsequently used to determine the near direct current (dc) reflectivity of $Cs_2AgBiBr_6$ at 50 Hz [panel (c)] to input in the Kramers-Kronig analysis. (d) Detail of ϵ_1 measured at 50 Hz near the 120 K transition exhibiting a slight hysteresis between cooling and warming given as blue triangles and red circles, respectively.

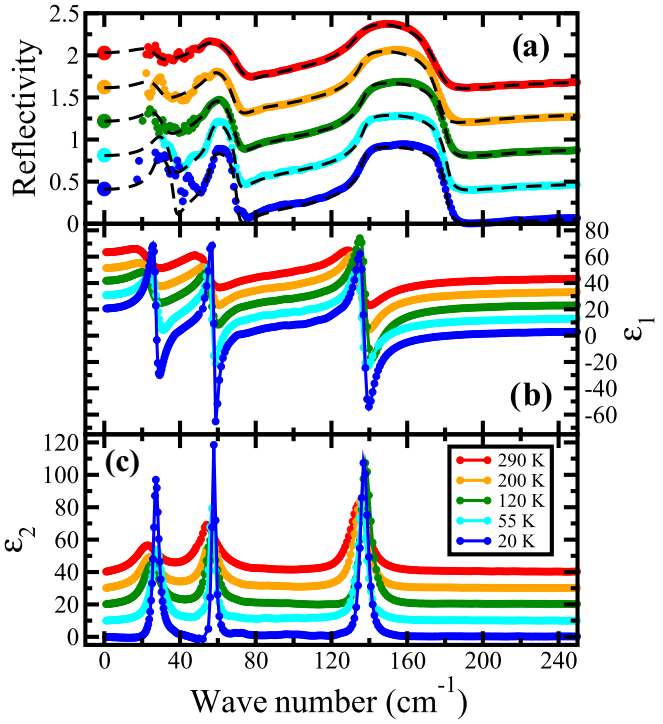


FIG. 10. (a) Reflectivity spectra of $Cs_2AgBiBr_6$ at select temperatures. Each subsequent curve is shifted by 0.4 for clarity. The dashed lines overlapping the experimental reflectivity curves are fits to the dielectric model [Eq. (7)]. The fit in the region 0–50 cm^{-1} aided by the near-dc (50 Hz) reflectivity obtained from the capacitance-loss measurements and shown as large solid circles was used to extrapolate the spectra for KK analyses. (b), (c) Corresponding real and imaginary parts, respectively, of the KK calculated dielectric function, similarly consecutively shifted by ten for clarity.

D. Infrared reflectivity

The temperature dependence of the IR reflectivity of an annealed single crystal of $Cs_2AgBiBr_6$ was measured with the goal of analyzing the IR-active modes in $Cs_2AgBiBr_6$. The reflectivity was measured using near-normal incidence conditions with the light propagating perpendicular to the (111) crystal face in the $Fm\bar{3}m$ cubic phase (see Fig. 1), which transforms to (101) in the tetragonal $I4/m$ phase and (100) in the proposed monoclinic $P12_1/n1$ phase. This should allow the observation of all IR-active phonons, as shown in Table IV; however, while a mode may be group theoretically predicted, actual oscillator strengths may be too weak to experimentally resolve.

Temperature-dependent spectra were obtained in a range from 20 to 11 000 cm^{-1}. Figure 10(a) shows typical reflectivity spectra in the far-infrared region of interest. As the low-intensity vibrational modes appear only very weakly in the reflectivity spectra, we performed a KK transformation to obtain clearly identifiable resonance features in the dielectric function. The magnitude of the reflectivity $\mathbf{R}(\omega)$ and the phase $\theta(\omega)$ are related via Eq. (6):

$$\theta(\omega) = -\frac{\omega}{\pi}\int_0^\infty d\Omega \frac{\ln(\mathbf{R}(\Omega)/\mathbf{R}(\omega))}{\Omega^2 - \omega^2}. \tag{6}$$

From the reflectivity and phase, the complex dielectric function [Eq. (5)] was determined. It may be noted that the KK integration necessitates a suitable choice of high- and low-frequency extrapolations.

Reflectivity data obtained from ellipsometry data measured by Jöbsis *et al.* [32] expanded the reflectivity to a range from 20 to 33 000 cm^{-1}. For more details, see Ref. [18]. To further extend the range to x-rays, a method described by Tanner [33] was employed. Tanner's method assumes an atomic number density weighted contribution using the elemental scattering factors to the dielectric function. The complex part of the scattering factors for the elements was obtained from Ref. [34] and the KK relations were applied to obtain the full scattering factor from which the x-ray reflectivity from 80 000 cm^{-1} to $\omega_{max} = 250\ 000\ 000\ cm^{-1}$ was obtained. The gap between UV to x-ray energies was modeled by using a cubic spline. Figure S2 of the Supplemental Material [18] provides an example of these extrapolations.

To extrapolate the high-frequency limit to infinity, the $R \propto \omega^{-4}$ relation was used. This corrects the phase at ω due to contributions from ω_{max} to ∞; details of this approach can be found in standard optical texts such as Appendix G of Wooten's *Optical Properties of Solids* [35].

The low-frequency extrapolation was guided by the number of expected IR-active modes. In the cubic phase, four such modes are expected. Although we observe these modes, the mode at $\sim$85 cm^{-1} is very weak, and the lowest-frequency mode occurs at $\sim$25 cm^{-1} in a region (20–50 cm^{-1}) of very low signal-to-noise ratio for the spectrometer used. The reflectivity spectra were fitted to the Lorentz dielectric model:

$$\tilde{\epsilon} = \epsilon_\infty + \sum_j^N \frac{f_j}{\omega_{oj}^2 - \omega^2 - i\gamma_j\omega}, \tag{7}$$

where ϵ_∞ accounts for high-frequency absorption processes beyond the spectral range and ω_{oj} are the frequencies of the oscillator contributions with corresponding scattering rates γ_j and oscillator strengths f_j. The resulting fits to the reflectance are given for select temperatures in Fig. 10(a). To keep the fit more physical in the low-frequency region without measured data, the model was forced to fit the "zero" frequency reflectivity, shown as large solid circles in Fig. 10(a), obtained via capacitance-loss measurements (50 Hz $\approx 2 \times 10^{-9}$ cm^{-1}). The fit in the range of 0–50 cm^{-1} was then used as the low-frequency extension for KK analysis. Choosing a suitable frequency range, the dielectric function was then extracted using KK analysis. The real and imaginary parts of $\tilde{\epsilon}$ are shown for select temperatures in FIGs. 10(b) and 10(c), respectively.

1. IR vibrational modes

In the cubic phase above 120 K with space group $Fm\bar{3}m$, group theory predicts four IR-active vibrational modes all of T_{1u} symmetry. Experimentally, three IR-active phonon modes are clearly visible in our spectra with frequencies of 25, 55, and $\sim$135 cm^{-1} (see Fig. 10) at room temperature. A fourth phonon mode (see below) occurs at $\sim$85 cm^{-1} at room temperature; however, it has a very low intensity and is just barely resolved in the reflectivity measurements, but is better observed in the dielectric function [see Fig. 11(a)]. The 25 cm^{-1} mode occurs in a region of low signal-to-noise ratio at low wave numbers. Its high-frequency tail is just observed.

Zelewski *et al.* [16] determined the phonon dispersion relations of $Cs_2AgBiBr_6$ in the cubic and the tetragonal phase by DFT calculations. Through analyzing the DFT calculated band diagrams at the Γ point, the frequencies of each mode were matched to the known Raman frequencies assuring the correct degeneracy leaving only the silent modes and IR-active modes unassigned. The frequencies of the IR-active modes were determined to be 30, 57, 99, and 149 cm^{-1}, agreeing quite well with our experimentally determined values. Rodrigues *et al.* used DFT calculations to determine the infrared reflectance and absorbance spectra of the the isotypic compound $Cs_2AgSbBr_6$ [15]. Clearly visible IR modes are found at 25, 80, and 212 cm^{-1}. Like in $Cs_2AgBiBr_6$, the fourth mode is very weak in intensity and located at $\sim$133 cm^{-1}. As expected for vibrational modes, the replacement of the heavier Bi by the lighter element Sb shifts the energies of the three highest IR modes to higher wave number, whereas the 25 cm^{-1} mode remains at the same energy. This is likely because the low-wave-number IR phonon is a collective mode involving the entire basis. Although all modes in the cubic structure possess T_{1u} symmetry and may therefore involve the full basis,

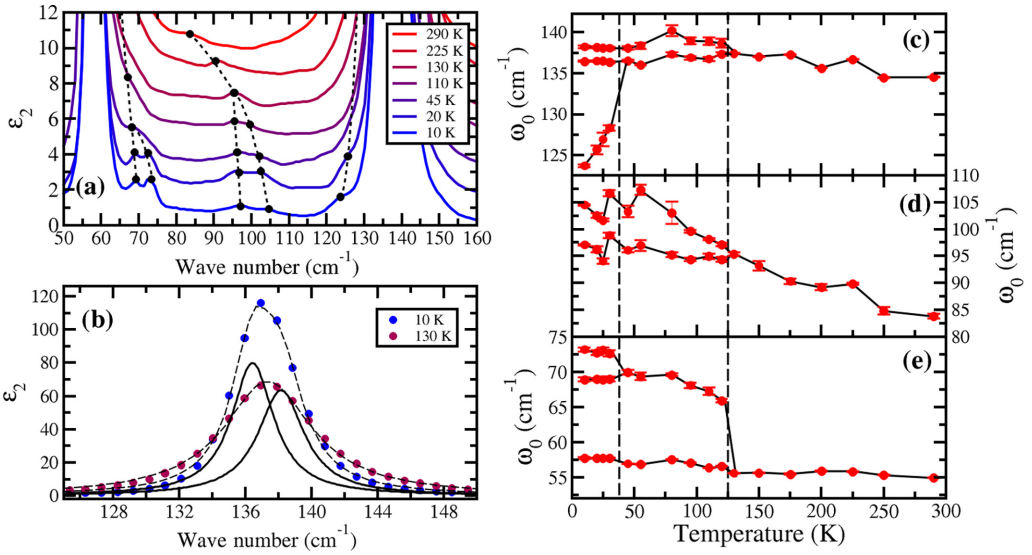


FIG. 11. (a) The KK extracted complex part of the dielectric function at select temperatures above and below the 38 and 120 K phase transitions. Black dots give the peak locations of fitting the phonon splitting of the three resolved T_{1u} to Eq. (7). Black dotted lines are to guide the eye to phonon splitting. (b) Example of Eq. (7) Lorentz fit of the 135 cm^{-1} phonon at 130 K in the cubic structure and 10 K in the monoclinic structure. Dashed lines indicate the fit, and solid lines show the fit components of the 10 K spectra. The splitting on the low-wave-number edge is not evident on this scale due to low intensity seen in panel (a). (c)–(e) Temperature evolution of the center frequency of the 135, 85, and 55 cm^{-1} phonons and splittings, obtained from Eq. (7) Lorentz fit. Vertical dashed lines indicate the 38 and 120 K phase transitions.

as the translational irreducible representation of each atomic site contributes, atomic displacement calculations based on a short-range force-field model for the double perovskite Ba_2MgWO_6 show that the low-wave-number mode has a larger contribution from the A-site cation (Cs in the case of $Cs_2AgBiBr_6$) relative to the higher-wave-number modes [36].

All of the IR-active modes in the ($m\bar{3}m$) cubic structure are T_{1u} triply degenerate modes that are expected to split into single and doubly degenerate A_u and E_u modes, respectively, in the (4/m) tetragonal phase (see Table IV). Experimentally, below 120 K, subtle evidence for splitting of the modes appears in the reflectivity data. Figure 12(a) shows a detail of the temperature dependence of the reflectance in the vicinity of the 55 cm^{-1} phonon. A small feature starts to develop on the high-frequency edge just above 70 cm^{-1} at temperatures below 120 K, as shown for 80 K in Fig. 12(b). The KK extracted dielectric function exhibits greater sensitivity to the vibrational modes, specifically the complex part, which displays more local behavior of the modes, compared to the more global effects of the reflectivity. Figures 12(c) and 12(d) show ϵ_1 and ϵ_2 in the vicinity of this mode. Figure 12(e) shows ϵ_2 in the spectral region corresponding to Figure 12(b), confirming that this feature is more prominent in the imaginary dielectric function. Figure 12(d) shows that a distinct peak is formed at 69 cm^{-1} at the lowest temperatures.

Simultaneous fitting of the Kramers-Kronig-derived dielectric function to the real and imaginary components of Eq. (7), followed by analysis of the peak positions, reveals clear splitting of the three highest-frequency experimentally resolved T_{1u} modes at 120 K [see Figs. 11(a) and 11(c)–11(e)]. Note that, as shown in Fig. 11(b), for the 135 cm^{-1} mode the splitting manifests as an asymmetry to the line shape below 120 K. In the cubic phase, a single Lorentzian is able to capture the line shape. Further splittings were observed at the 40 K phase transition.

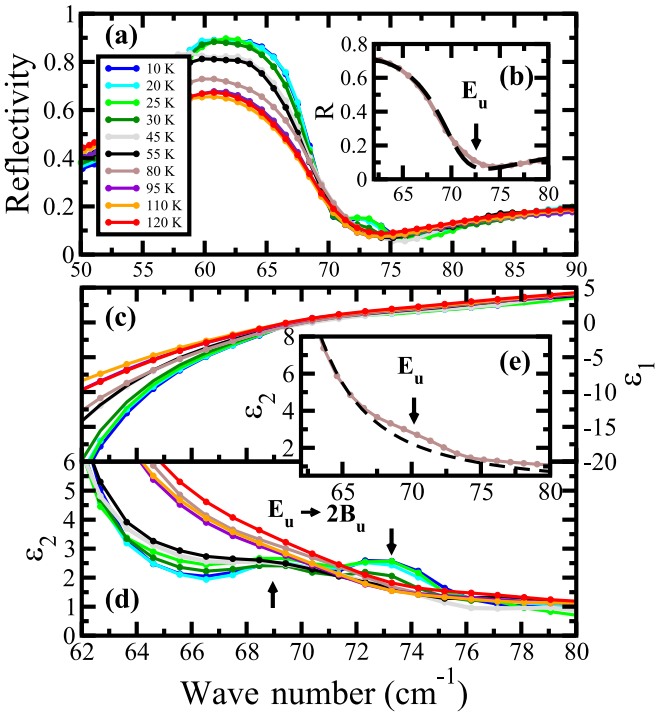


FIG. 12. Details of the reflectivity [panel (a)] and the KK extracted dielectric function [panels (c) and (d)] below 120 K around the 69 cm^{-1} E_u phonon that splits from the T_{1u} mode ($T_{1u} \rightarrow A_u + E_u$). The insets show, as an example for 80 K, the 69 cm^{-1} E_u mode detected in the tetragonal phase as a deviation from the Lorentz dielectric model fit to the four phonon modes of the cubic phase (dashed black lines) for both the reflectivity [panel (b)] and complex part of the dielectric function [panel (e)]. It is just barely discernible from the large tail of the 55 cm^{-1} phonon. Below the 40 K transition, another mode appears near 73 cm^{-1}, believed to be the E_u mode splitting into two B_u modes under monoclinic symmetry.

2. 40 K phase transition

Predicated upon our PXRD results, a symmetry lowering below ∼40 K is clearly supported. The monoclinic and triclinic space groups considered in our discussion of the PXRD results below 40 K would all result in an increase in the number of IR-active modes. For the monoclinic space group $P12_1/n1$, group theory predicts $17A_u$ and $16B_u$ modes, whereas for the monoclinic space group $I12/m1$ 15 IR-active modes ($5A_u + 10B_u$) are expected. For the triclinic space group $I\bar{1}$, group theory also predicts 15 modes of A_u symmetry [37–40].

Strong support for a monoclinic $P12_1/n1$ symmetry of the low-temperature crystal structure of $Cs_2AgBiBr_6$ can be derived from the distinct increase of the number of Raman modes observed by Cohen *et al.* whose measurements suggest a total of 24 Raman-active modes [11]. Group theory predicts for the monoclinic $I2/m$ structure only 12 Raman-active modes ($6A_g + 6B_g$). Similarly, the triclinic $I\bar{1}$ structure only gives 12 Raman-active modes ($12A_g$), whereas for the space group $P12_1/n1$ 24 Raman modes are expected ($12A_g + 12B_g$), in quantitative agreement with Cohen *et al.*'s findings.

Note that the number of modes given above for the $I12/m1$, $I\bar{1}$, and $P12_1/n1$ space groups corresponds to the unit cells of Table I, which agree with the number of modes of known oxide and halide double perovskites that form in these space groups such as Sr_2ScSbO_6 with an $I12/m1$ to $P12_1/n1$ transition and Rb_2KScF_6 with an $I4/m$ to $P12_1/n1$ transition [41,42]. A 40-atom (20 atoms in the primitive cell) $I\bar{1}$ or $I2/m$ cell could also give 24 Raman-active modes with possible

TABLE III. Wyckoff sites of $Cs_2AgBiBr_6$ in $Fm\bar{3}m$ (cubic), $I4/m$ (tetragonal), and $P12_1/n1$ (monoclinic) space groups. Possible Wyckoff positions for $I12/m1$ and $I\bar{1}$ structures that would give 24 Raman-active modes are also listed. The Wyckoff positions in braces are the Wyckoff symbols of $P2_1/n$ in the standard setting of group 14 ($P2_1/c$).

	$Fm\bar{3}m$	$I4/m$	$P2_1/n$ $\{P2_1/c\}$	$I2/m$	$I\bar{1}$
Cs	8c	4d	4e {4e}	8j	4i (2x)
Ag	4b	2b	2b {2d}	2b, 2d	2d, 2g
Bi	4a	2a	2a {2a}	2a, 2c	2b, 2e
Br	24e	8h, 4e	4e {4e} (3x)	4i (4x), 4g, 4h	4i (6x)

structures for these groups given by the Wyckoff sites in Table III. This would, however, require a substantial increase in the number of free parameters compared to the $I12/m1$ and $I\bar{1}$ refinements given in Table I, and therefore, although we cannot explicitly eliminate them, we are inclined to suggest that they are not as favored as $P12_1/n1$.

To identify the IR modes expected at low temperature, we again consider Table IV, where the (2/m) columns correspond to $P12_1/n1$. Reading across the row starting with the IR-active T_{1u} in the cubic structure ($m\bar{3}m$), we see that each T_{1u} mode splits into an A_u mode and an E_u mode in the tetragonal structure (4/m). The doubly degenerate E_u mode further splits in the monoclinic structure (2/m) such that at the lowest temperatures one A_u mode and two B_u modes are expected. The resolution of a typical low-temperature far-infrared spectroscopy measurement limits the ability to observe small splittings and weaker modes. In Fig. 10(a), in the 20 K reflectivity spectrum there is, however, experimental evidence of an additional mode at $\approx$73 cm^{-1} for temperatures below 40 K, which can be seen more clearly in Fig. 12(a) at temperatures below 40 K. This mode is assigned to the further splitting of the $\approx$69 cm^{-1} E_u mode that splits from the 55 cm^{-1} T_{1u} mode at 120 K. This splitting is more distinguishable in the KK extracted dielectric function shown in Fig. 11, which shows $E_u \rightarrow 2B_u$ splitting of the 55 and 135 cm^{-1} modes below 40 K. Further splitting of the weak 85 cm^{-1} mode below 40 K could not be resolved.

IV. CONCLUSION

In summary, we have investigated thermal, structural, dielectric, and infrared optical properties of the bromide double perovskite $Cs_2AgBiBr_6$. Our low-temperature x-ray investigations and the IR reflectivity spectra provide compelling evidence that apart from the thoroughly investigated cubic-to-tetragonal structural phase transition at $\sim$120 K in $Cs_2AgBiBr_6$, another low-temperature structural phase transition takes place at $\sim$40 K, which leads to a symmetry lowering of the crystal structure. Our x-ray powder diffraction data point to a monoclinic or triclinic crystal structure of the low-temperature phase with a slight preference—judging from the somewhat reduced reliability factors—to a triclinic $I\bar{1}$ description. Our findings regarding the temperature dependence of the cell volume substantiate the report by Keshavarz *et al.* [10] who observed a thermal expansion anomaly at $\sim$40 K. Our results concur in part with the findings of He *et al.* in that the transition involves a more complex network of the Bi-Br octahedrals as the structure is altered below the 40 K transition; however, we suggest based on our infrared and literature Raman spectra that this structural transition is the symmetry lowering from $I4/m$ to $P12_1/n1$ rather than to a several hundred atom unit cell as predicted by their DFT modeling.

The appearance of additional IR-active modes is consistent with a lower symmetry for the low-temperature crystal structure. All monoclinic or triclinic descriptions induce a growth of the number of IR-active modes. The monoclinic and the triclinic description refinements to the PXRD patterns of the low-temperature phase are almost equally good. The somewhat reduced reliability factors favor the triclinic description. The symmetry of perovskite structures is often over- or underestimated [43]; however, judging from the significantly increased number of Raman modes

TABLE IV. Vibrational mode splitting in the three phases of $Cs_2AgBiBr_6$ $Fm\bar{3}m$, $I4/m$, and $P2_1/c$ given by grouped rows. Raman active, IR active, acoustic, and silent modes are italic text, bold text, marked with an asterisk, and marked with a dagger respectively. Blank rows for point groups $m\bar{3}m$ and $4/m$ indicate additional modes in the $2/m$ symmetry from a primitive cell doubling from $I4/m$ to $P2_1/c$. Listed beside each mode is the corresponding linear or quadratic basis function if applicable, and the Wyckoff sites that may contribute to the mode.

Mode Irr Rep	$m\bar{3}m$ Basis Fnc	Wyckoff	$4/m$			$2/m$		
A_{1g}	$x^2+y^2+z^2$	24e	A_g	x^2+y^2,z^2	8h (2x), 4e	A_g	x^2,y^2,z^2, xy	4e (3x)
E_g	$(2z^2-x^2-y^2, x^2-y^2)$	24e	A_g	x^2+y^2,z^2	8h (2x), 4e	A_g	x^2,y^2,z^2, xy	4e (3x)
			B_g	xy, x^2-y^2	8h (2x), 4d	A_g	x^2,y^2,z^2, xy	4e (3x)
$2T_{2g}$	(xy, xz, yz)	8c, 24e	$2B_g$	xy, x^2-y^2	8h (2x), 4d	$2A_g$	x^2,y^2,z^2, xy	4e (3x)
			$2E_g$	(xz, yz)	8h, 4e, 4d	$4B_g$	xz, yz	4e (3x)
$4\mathbf{T}_{1u}$	(x, y, z)	8c, 4b, 4a, 24e (2x)	$4\mathbf{A}_u$	z	8h, 4e, 4d, 2b, 2a	$4\mathbf{A}_u$	z	4e (3x), 2d (3x), 2a (3x)
			$4\mathbf{E}_u$	(x, y)	8h (2x), 4e, 4d, 2b, 2a	$8\mathbf{B}_u$	x, y	4e (3x), 2d (3x), 2a (3x)
$T_{1u}{}^*$	(x, y, z)	8c, 4b, 4a, 24e (2x)	$A_u{}^*$	z	8h, 4e, 4d, 2b, 2a	$A_u{}^*$	z	4e (3x), 2d (3x), 2a (3x)
			$E_u{}^*$	(x, y)	8h (2x), 4e, 4d, 2b, 2a	$2B_u{}^*$	x, y	4e (3x), 2d (3x), 2a (3x)
$T_{1g}{}^\dagger$		24e	A_g	x^2+y^2,z^2	8h (2x), 4e	A_g	x^2, y^2,z^2, xy	4e (3x)
			E_g	(xz, yz)	8h, 4e, 4d	$2B_g$	xz, yz	4e (3x)
$T_{2u}{}^\dagger$		24e	$B_u{}^\dagger$		8h	$\mathbf{A}_u$	z	4e (3x), 2d (3x), 2a (3x)
			$\mathbf{E}_u$	(x, y)	8h (2x), 4e, 4d, 2b, 2a	$2\mathbf{B}_u$	x, y	4e (3x), 2d (3x), 2a (3x)
						$6A_g$	x^2, y^2, z^2, xy	4e (3x)
						$6B_g$	xz, yz	4e (3x)
						$12\mathbf{A}_u$	z	4e (3x), 2d (3x), 2a (3x)
						$6\mathbf{B}_u$	x, y	4e (3x), 2d (3x), 2a (3x)

found by Cohen *et al.* [11], which is in quantitative agreement with that expected for the monoclinic space group $P12_1/n1$, we suggest that $P12_1/n1$ provides the more consistent description of the crystal structure of $Cs_2AgBiBr_6$ below ∼40 K.

ACKNOWLEDGMENTS

We acknowledge the support of Brock University and the Natural Sciences and Engineering Research Council of Canada Discovery Grants program (Funding Reference No. RGPIN-2022-05214). Scholarship funding was provided to C.T. from the Canada Graduate Research Scholarship – Doctoral program and J.D. from the Ontario Graduate Scholarship Program.

DATA AVAILABILITY

The data that support the findings of this article are not publicly available upon publication because it is not technically feasible and/or the cost of preparing, depositing, and hosting the data

would be prohibitive within the terms of this research project. The data are available from the authors upon reasonable request.

[1] K. Fu, A. Ho-Baillie, H. K. Mulmudi, and P. T. T. Trang, *Perovskite Solar Cells* (Apple Academic Press, Oakville, On, Canada, 2019).

[2] Q. Hu, Z. Deng, M. Hu, A. Zhao, Y. Zhang, Z. Tan, G. Niu, H. Wu, and J. Tang, X-ray scintillation in lead-free double perovskite crystals, Sci. China Chem. **61**, 1581 (2018).

[3] T. Ava, A. Mamun, S. Marsillac, and G. Namkoong, A review: Thermal stability of methylammonium lead halide based perovskite solar cells, Appl. Sci. **9**, 188 (2019).

[4] A. Slavney, T. Hu, A. Lindenberg, and H. Karunadasa, A bismuth-halide double perovskite with long carrier recombination lifetime for photovoltaic applications, J. Am. Chem. Soc. **138**, 2138 (2016).

[5] Y. Wang, T. Zhang, M. Kan, Y. L. T. Wang, and Y. Zhao, Efficient α-$CsPbI_3$ photovoltaics with surface terminated organic cations, Joule **2**, 2065 (2018).

[6] P. Sun, Q. Li, L. Yang, and Z. Li, Theoretical insights into a potential lead-free hybrid perovskite: Substituting Pb^{2+} with Ge^{2+}, Nanoscale **8**, 1503 (2016).

[7] E. McClure, M. Ball, W. Windl, and P. Woodward, $Cs_2AgBiBr_6$(X = Br, Cl): New visible light absorbing, lead-free halide perovskite semiconductors, Chem. Mater. **28**, 1348 (2016).

[8] F. Igbari, Z. Wang, and L. Liao, Progress of lead-free halide double perovskites, Adv. Energy Mater. **9**, 1803150 (2019).

[9] L. Schade, A. Wright, R. Johnson, M. Dollmann, B. Wenger, P. Nayak, D. Prabhakaran, L. Herz, R. Nicholas, H. Snaith, and P. Radaelli, Structural and optical properties of $Cs_2AgBiBr_6$ double perovskite, ACS Energy Lett. **4**, 299 (2019).

[10] M. Keshavarz, E. Debroye, M. Ottesen, C. Martin, H. Zhang, E. Fron, R. Kuechler, J. A. Steele, M. Bremholm, J. Van de Vondel, H. Wang, I. M. Bonn, M. B. J. Roeffaers, S. Wiedmann, and J. Hofkens, Tuning the structural and optoelectronic properties of $Cs_2AgBiBr_6$ double-perovskite single crystals through alkali-metal substitution, Adv. Mater. **32**, 2001878 (2020).

[11] A. Cohen, T. M. Brenner, J. Klarbring, R. Sharma, D. H. Fabini, R. Korobko, P. K. Nayak, O. Hellman, and O. Yaffe, Diverging expressions of anharmonicity in halide perovskites, Adv. Mater. **34**, 2107932 (2022).

[12] X. He, M. Krogstad, M. K. Gupta, T. Lanigan-Atkins, C. Mao, F. Ye, Y. Liu, T. Hong, S. Chi, H. Wei, J. Huang, S. Rosenkranz, R. Osborn, and O. Delaire, Multiple lattice instabilities and complex ground state in $Cs_2AgBiBr_6$, PRX Energy **3**, 013014 (2024).

[13] J. Zheng, C. Lin, C. Lin, G. Hautier, R. Guo, and B. Huang, Unravelling ultralow thermal conductivity in perovskite $Cs_2AgBiBr_6$: Dominant wave-like phonon tunnelling and strong anharmonicity, npj Comput. Mater. **10**, 30 (2024).

[14] J. Klarbring, O. Hellman, I. Abrikosov, and S. Simak, Anharmonicity and ultralow thermal conductivity in lead-free halide double perovskites, Phys. Rev. Lett. **125**, 045701 (2020).

[15] J. Rodrigues, C. Escanhoela, G. S. B. Fragoso, M. Ferrer, C. Ánlvarez Galván, M. Fernánndez-Díaz, J. Souza, F. Ferreira, C. Pecharromán, and J. A. Alonso, Experimental and theoretical investigations on the structural, electronic, and vibrational properties of $Cs_2AgSbCl_6$ double perovskite, Ind. Eng. Chem. Res. **60**, 18918 (2021).

[16] S. J. Zelewski, J. M. Urban, A. Surrente, D. K. Maude, A. Kuc, L. Schade, R. D. Johnson, M. Dollmann, P. K. Nayak, H. J. Snaith, P. Radaelli, R. Kudrawiec, R. J. Nicholas, P. Plochocka, and M. Baranowski, Revealing the nature of photoluminescence emission in the metal-halide double perovskite $Cs_2AgBiBr_6$, J. Mater. Chem. C **7**, 8350 (2019).

[17] L. Yin, H. Wu, W. Pan, B. Yang, P. Li, G. N. J. Luo, and J. Tang, Controlled cooling for synthesis of $Cs_2AgBiBr_6$ single crystals and its application for x-ray detection, Adv. Opt. Mater. **7**, 1900491 (2019).

[18] See Supplemental Material at https://link.aps.org/supplemental/10.1103/fs84-8lgj for information regarding synthesis, experimental techniques used, a discussion of water contamination of the MIR reflectance

spectrum, phase transitions in double perovskites, the results of the low-temperature single-crystal x-ray diffraction measurements, and powder transmission measurements, which includes Refs. [44–58].

[19] J. Rodríguez-Carvajal, Recent advances in magnetic structure determination by neutron powder diffraction, Physica B **192**, 55 (1993).

[20] G. Cakmak, J. Nuss, and M. Jansen, LiB_6O_9F, the first lithium fluorooxoborate—Crystal structure and ionic conductivity, Z. Anorg. Allg. Chem. **635**, 631 (2009).

[21] Bruker Suite, version 2019/1, Bruker AXS Inc., Madison, WI, 2019.

[22] G. M. Sheldrick, Sadabs Bruker-AXS area detector scaling and absorption, version 2016/2, University of Göttingen, 2016.

[23] G. M. Sheldrick, A short history of *SHELX*, Acta Crystallogr., Sect. A **64**, 112 (2008).

[24] G. M. Sheldrick, Crystal structure refinement with *SHELXL*, Acta Crystallogr., Sect. C **71**, 3 (2015).

[25] V. Petříček, M. Dušek, and L. Palatinus, Crystallographic computing system Jana2006: General features, Z. Kristallogr.—Cryst. Mater. **229**, 345 (2014).

[26] C. Homes, M. Reedyk, D. Crandles, and T. Timusk, Technique for measuring the reflectance of irregular, submillimeter-sized samples, Appl. Opt. **32**, 2976 (1993).

[27] W. Schnelle, J. Engelhardt, and E. Gmelin, Specific heat capacity of Apiezon N high vacuum grease and of Duran borosilicate glass, Cryogenics **39**, 271 (1999).

[28] A. Le Bail, Whole powder pattern decomposition methods and applications: A retrospection, Powder Diffr. **20**, 316 (2005).

[29] A. L. Spek, Single-crystal structure validation with the program PLATON, Journal of Applied Crystallography **36**, 7 (2003).

[30] Z. Zhang, P. M. Gehring, A. H. Slavney, J. A. Vigil, T. Hong, J. A. Rodriguez-Rivera, J. Klarbring, H. I. Karunadasa, M. F. Toney, and N. J. Weadock, Phonon lifetimes and mode softening in cubic $Cs_2AgBiBr_6$, Newton **1**, 100097 (2025).

[31] J. Scott, Soft-mode spectroscopy: Experimental studies of structural phase transitions, Rev. Mod. Phys. **46**, 83 (1974).

[32] H. Jöbsis, V. M. Caselli, S. H. C. Askes, E. C. Garnett, T. J. Savenije, F. T. Rabouw, and E. M. Hutter, Recombination and localization: Unfolding the pathways behind conductivity losses in $Cs_2AgBiBr_6$ thin films, Appl. Phys. Lett. **119**, 131908 (2021).

[33] D. Tanner, Use of X-ray scattering functions in Kramers-Kronig analysis of reflectance, Phys. Rev. B **91**, 035123 (2015).

[34] B. Henke, E. Gullikson, and J. Davis, X-ray interactions: Photoabsorption, scattering, transmission, and reflection at $E = 50$–$30{,}000$ eV, $Z = 1$–92, At. Data Nucl. Data Tables **54**, 181 (1993).

[35] F. Wooten, *Optical Properties of Solids* (Academic Press, New York, NY, 1972).

[36] J. Rodrigues, D. Bezerra, and A. Hernandes, Calculation of the optical phonons in ordered ba_2mgwo_6 perovskite using short-range force field model, J. Raman Spectrosc. **49**, 1822 (2018).

[37] M. I. Aroyo, J. M. Perez-Mato, D. Orobengoa, E. Tasci, G. de la Flor, and A. Kirov, Crystallography online: Bilbao Crystallographic Server, Bulg. Chem. Commun. **43**, 183 (2011).

[38] M. I. Aroyo, J. M. Perez-Mato, C. Capillas, E. Kroumova, S. Ivantchev, G. Madariaga, A. Kirov, and H. Wondratschek, Bilbao Crystallographic Server I: Databases and crystallographic computing programs, Z. Kristallogr. **221**, 15 (2006).

[39] M. I. Aroyo, A. Kirov, C. Capillas, J. M. Perez-Mato, and H. Wondratschek, Bilbao Crystallographic Server II: Representations of crystallographic point groups and space groups, Acta Crystallogr., Sect. A **62**, 115 (2006).

[40] E. Kroumova, M. I. Aroyo, J. M. P. Mato, A. Kirov, C. Capillas, S. Ivantchev, and H. Wondratschek, Bilbao Crystallographic Server: Useful databases and tools for phase transitions studies, Phase Transitions **76**, 155 (2003).

[41] A. Faik, D. Orobengoa, E. Iturbe-Zabalo, and J. Igartua, A study of the crystal structures and the phase transitions of the ordered double perovskites Sr_2ScSbO_6 and Ca_2ScSbO_6, J. Solid State Chem. **192**, 273 (2012).

[42] I. Flerov, R. Burriel, M. Gorev, P. Isla, and V. Voronov, Low-temperature specific heat of the Rb_2KScF_6 elpasolite, Phys. Solid State **45**, 167 (2003).

[43] C. J. Howard, B. J. Kennedy, and P. M. Woodward, Ordered double perovskites; a group-theoretical analysis, Acta Crystallogr., Sect. B: Struct. Sci. **59**, 463 (2003).

[44] Z. Weng, J. Qin, A. A. Umar, J. Wang, X. Zhang, H. Wang, X. Cui, X. Li, L. Zheng, and Y. Zhan, Lead-free $Cs_2AgBiBr_6$ double perovskite-based humidity sensor with superfast recovery time, Adv. Funct. Mater. **29**, 1902234 (2019).

[45] B.-H. Wang, B. Gao, J.-R. Zhang, L. Chen, G. Junkang, S. Shen, C.-T. Au, K. Li, M.-Q. Cai, and S.-F. Yin, Thickness-induced band-gap engineering in lead-free double perovskite $Cs_2AgBiBr_6$ for highly efficient photocatalysis, Phys. Chem. Chem. Phys. **23**, 12439 (2021).

[46] E. Bartalucci, A. A. Malär, A. Mehnert, J. B. Kleine Büning, L. Günzel, M. Icker, M. Börner, C. Wiebeler, B. H. Meier, S. Grimme, *et al.*, Probing a hydrogen-π interaction involving a trapped water molecule in the solid state, Angew. Chem. Int. Ed. **62**, e202217725 (2023).

[47] J. Liu, Z. Wu, F. Zhang, M. Zhao, C. Li, J. Li, B. Wen, and F. Wang, *In situ* growth of lead-free halide perovskites into SiO_2 sub-microcapsules toward water-stable photocatalytic CO_2 reduction, Nanoscale **15**, 7023 (2023).

[48] D. M. Jöckel, S. Yoon, A. Frebel, S. M. Neguse, J. D. Rossa, A. J. Bett, M. Schubert, M. Widenmeyer, B. Balke-Grünewald, and A. Weidenkaff, Solar degradation and stability of lead-free light absorber $Cs_2AgBiBr_6$ in ambient conditions, Adv. Photonics Res. **5**, 2300269 (2024).

[49] S. Vasala and M. Karppinen, $A_2B'B''O_6$ perovskites: A review, Prog. Solid State Chem. **43**, 1 (2015).

[50] W. Fu, R. Götz, and D. Ijdo, On the symmetry and crystal structures of Ba_2LaIrO_6, J. Solid State Chem. **183**, 419 (2010).

[51] P. Battle, The crystal structures of Ba_2LaRuO_6 and Ca_2LaRuO_6, Mater. Res. Bull. **16**, 397 (1981).

[52] P. Battle, J. Goodenough, and R. Price, The crystal structures and magnetic properties of Ba_2LaRuO_6 and Ca_2LaRuO_6, J. Solid State Chem. **46**, 234 (1983).

[53] Q. Zhou, B. J. Kennedy, M. Avdeev, L. Giachini, and J. A. Kimpton, Structural studies of the phases in Ba_2LaIrO_6—New light on an old problem, J. Solid State Chem. **182**, 3195 (2009).

[54] F. Ji, J. Klarbring, F. Wang, W. Ning, L. Wang, C. Yin, J. S. M. Figueroa, C. K. Christensen, M. Etter, T. Ederth, L. Sun, S. I. Simak, I. A. Abrikosov, and F. Gao, Lead-free halide double perovskite $Cs_2AgBiBr_6$ with decreased band gap, Angew. Chem. Int. Ed. **59**, 15191 (2020).

[55] P. Sikarwar, P. Siwach, N. V. Phani Chandra, S. Antharjanam, and A. K. Chandiran, Dimensional reduction of $Cs_2AgBiBr_6$ using alkyl ammonium cations $CH_3(CH_2)_nNH_3^+$ ($n = 1, 2, 3$, and 6) of varying chain lengths and their role in structural and optoelectronic properties, Inorg. Chem. **62**, 5836 (2023) (the referenced data is found in the CIF files of the data availability section).

[56] J. D. Dunitz, V. Schomaker, and K. N. Trueblood, Interpretation of atomic displacement parameters from diffraction studies of crystals, J. Phys. Chem. **92**, 856 (1988).

[57] J. A. Stratton, I. Antennas, and P. Society, *Electromagnetic Theory* (John Wiley & Sons, Inc., Hoboken, NJ, 2015).

[58] H. Weber, The Fresnel equations for lossy dielectrics and conservation of energy, J. Mod. Opt. **61**, 1219 (2014).